Japanese Journal of Applied Physics

The Japan Society of Applied Physics

REGULAR PAPERS

Ultra-thin dielectric insertions for contact resistivity lowering in advanced CMOS: Promises and challenges

To cite this article: Julien Borrel *et al* 2017 *Jpn. J. Appl. Phys.* **56** 04CB02

Japanese Journal of Applied Physics **56**, 04CB02 (2017) **REGULAR PAPER**
https://doi.org/10.7567/JJAP.56.04CB02

Ultra-thin dielectric insertions for contact resistivity lowering in advanced CMOS: Promises and challenges

Julien Borrel[1,2,3*], Louis Hutin[1], Donato Kava[4], Remy Gassilloud[1], Nicolas Bernier[1], Yves Morand[2], Fabrice Nemouchi[1], Magali Gregoire[2], Emmanuel Dubois[3], and Maud Vinet[1]

[1]*CEA, LETI, Minatec Campus, F-38054 Grenoble, France*
[2]*STMicroelectronics, 850 Rue Jean Monnet, 38926 Crolles, France*
[3]*IEMN, UMR 8520 CNRS, Avenue Poincaré, BP 60069, 59652 Villeneuve D'Ascq Cedex, France*
[4]*Department of Electrical and Computer Engineering, University of Texas at El Paso, El Paso, TX 79968, U.S.A.*

*E-mail: julien.borrel@cea.fr

Received October 12, 2016; revised December 16, 2016; accepted January 2, 2017; published online February 21, 2017

In this paper, in order to provide a comprehensive overview of the opportunities and limitations of the metal/insulator/semiconductor contacts approach, expected performance based on ideal contact simulations as well as key practical aspects are presented. While the former give us a glimpse of the theoretical potential of this paradigm, mainly to contact nFETs, the latter highlights concerns about the electrical characterization of such contacts along with issues occurring during their physical implementation.

1. Introduction

Due to Fermi level pinning (FLP), the effective metal workfunctions on metal/semiconductor contacts are almost independent from their reference value,[1)] hindering proper optimization of the contact resistivity lowering. It was shown[2)] that one way to mitigate the FLP could consist in inserting a dielectric layer between the metal and the semiconductor. Obviously a trade-off arises from the competition between the induced tunneling resistance and the Schottky barrier height (SBH) reduction, hence defining an optimal dielectric thickness. The magnitude of this tunnel resistance is related to conduction and valence band offsets[3)] which are presented in Fig. 1.

Using one-dimensional (1D) analytical simulations, stand-alone current density–voltage (J–V) characteristics of metal/insulator/semiconductor (MIS) contacts were generated allowing screening the performance of such contacts as a function of the doping concentration of the substrate, the nature and the thickness of the dielectric and the nature of the metallization. Including these results in SPICE simulations, their impact on DC and AC MOSFETs performance were also evaluated.

Subsequently, issues occurring during the practical implementation and the electrical characterization of MIS contacts are presented since they respectively prevent from obtaining expected functioning ideal stack and from properly evaluating their performance.

2. Simulation foresights

Before physically implementing various types of MIS stacks, first screenings of their potential individual properties and of their impact on devices were performed using simulations. The former was completed in Ref. 6 using 1D analytical simulation and was used to analyze physical and fundamental aspects of the MIS approach. The calculation of the current density as a function of the contact bias (J–V) was performed using the algorithm described in Fig. 2. For the sake of simplicity, the algorithm is not presented in the following but an extensive explanation can be found in Ref. 6.

The latter that is evaluating the impact of MIS contacts on devices, required SPICE and TCAD simulations and was more focused on forecasting operating issues. An extensive presentation of this work is developed in Ref. 7.

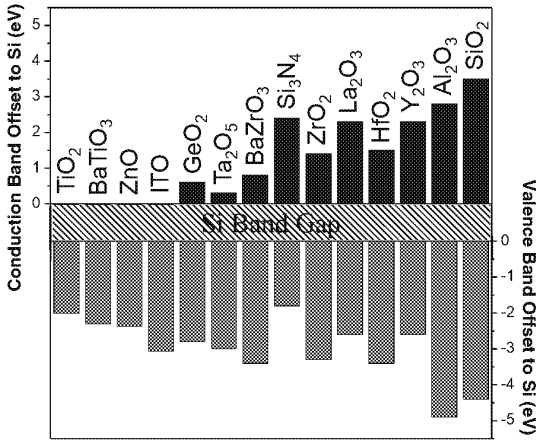

Fig. 1. (Color online) Conduction and valence band offsets of various dielectrics.[4,5)] The tunneling resistance of a dielectric is strongly correlated to them.

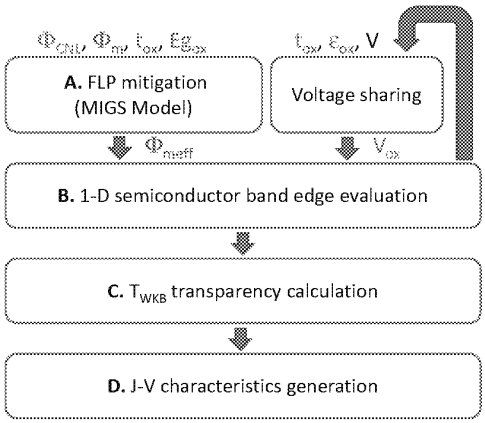

Fig. 2. (Color online) Algorithm used for J–V calculations.[6)] The MIGS attenuation-based FLP alleviation and the SBH image force lowering were considered.

Table I. Main parameters used in current simulations for common materials.[4)]

Dielectric	Band gap E_g (eV)	Relative permittivity ε_{IL}	Relative mass m^*	Conduction band offset ΔE_c/Si (eV)	Valence band offset ΔE_v/Si (eV)
SiO_2	9	3.9	0.3	3.5	4.4
Al_2O_3	8.8	9	0.2	2.8	4.9
Si_3N_4	5.3	7	0.2	1.9	1.8
TiO_2	3.05	80	0.3	−0.06	2.01

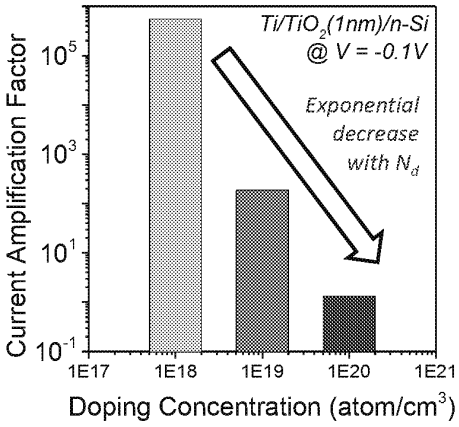

Fig. 3. (Color online) Current amplification at −0.1 V induced by a 1 nm TiO_2 interlayer as a function of the dopant concentrations.[11)]

Aiming at finding realistic solutions in an industrial clean room environment, standard dielectric insertions (Al_2O_3, Si_3N_4, and TiO_2) and capping metallizations (Zr, Ti, and Pt) were considered. Concerning the dielectrics insertions, the main parameters used for the simulations are presented in Table I and are taken from Ref. 4. For their part, the ideal metal workfunction values of Zr, Ti, and Pt were respectively 4.05, 4.33, and 5 eV (resp. Refs. 8, 9, and 10).

2.1 Doping concentration impact

In Ref. 11, a first simulation study was dedicated to evaluate the influence of the substrate doping concentration on the properties of a given M, I, and S combination. *J–V* simulation was applied for a $Ti/TiO_2/Si$ contact. The insertion thickness was set at 1 nm and n-Si doping concentrations of $N_d = 10^{18}$, 10^{19}, and 10^{20} atoms/cm^3 were considered.

Using the module of the algorithm dedicated to evaluate the FLP attenuation for a given contact (module A in Fig. 2), effective SBHs of 0.23, 0.29, and 0.35 eV were found for the different Si doping concentrations. Considering all these inputs parameters, the current amplification factor, as defined in Eq. (1), was generated as a function of the doping concentration and is presented in Fig. 3.

$$\text{Current amplification factor } (t_{TiO_2}) = \frac{\text{Current of Ti/TiO}_2(t_{TiO_2})\text{/Si contact}}{\text{Current of Ti/Si contact}} \quad (1)$$

It appears that while the current is multiplied by a factor of 10^6 when inserting a 1-nm-thick TiO_2 layer between the Ti metallization and a 10^{18} atoms/cm^3 n-doped Si, the amplification factor drops down to unity on a 10^{20} atoms/cm^3 doped Si.

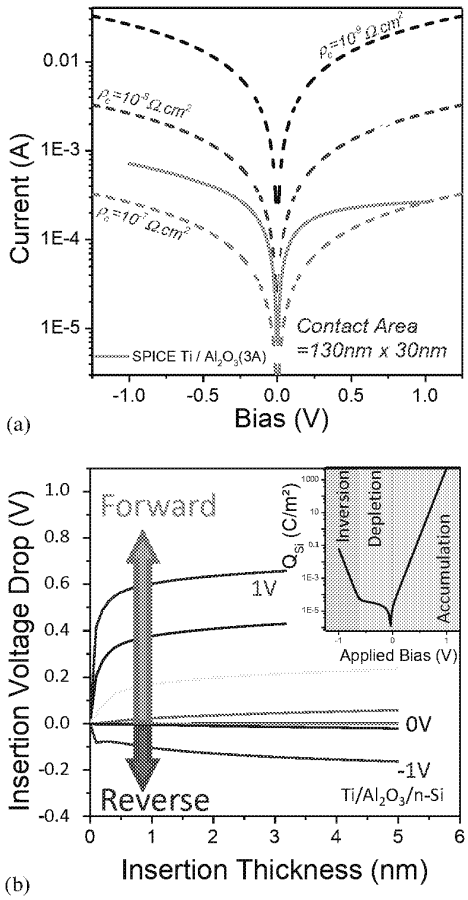

Fig. 4. (Color online) (a) *I–V* characteristic (log scale) of emulated MIS and ohmic contacts, showing the current drop for high values of forward bias. (b) Voltage drop occurring in the Al_2O_3 insertion as a function of the insertion thickness and the applied bias for a Ti metallization. Inset: Semiconductor surface charge as the function of the applied bias.[6)]

This tremendous degradation of the current amplification factor is mainly due to the difference of transport mechanisms occurring at the interface between a lowly doped Si based contact and a highly doped one. At low doping concentration, the carrier emission being nearly purely thermionic, even a slight modification of the SBH can result in a high reverse-bias current enhancement. Therefore, the tunneling resistance induced as the dielectric thickness increases is largely counterbalanced by the diminution of the SBH.

However, contacts will realistically be made on degenerately doped source and drain in order to meet the industrial requirements. Therefore, the expected current gain is more modest since the relative importance of field emission tunneling current is greater and the tunneling resistance induced by the dielectric can no longer be compensated by increasing the thermionic conductivity.

2.2 Non-linearity

Additional simulation studies[6)] performed on various combinations of M, I, and S have also shown that MIS contacts are inherently neither linear nor symmetrical in a [−1 V; +1 V] bias range. As an example, the current–voltage (*I–V*) characteristics of a Ti/Al_2O_3-based contact is plotted in Fig. 4(a) as a function of the applied bias. The associated dielectric voltage drop is shown in Fig. 4(a) along with ideal ohmic

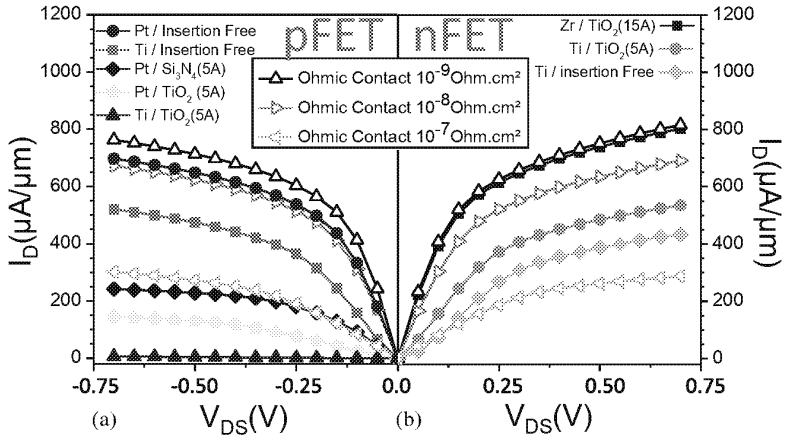

Fig. 5. (Color online) Simulated scaled (a) p- and (b) n-MOSFET ($L_g = 18$ nm, $W = 130$ nm) drain current as a function of V_{DS} for ohmic and MIS contacts assuming $q\Phi_m(\mathrm{Zr}) = 4.1$ eV, $q\Phi_m(\mathrm{Ti}) = 4.33$ eV, and $q\Phi_m(\mathrm{Pt}) = 5$ eV.[13]

references of 10^{-7}, 10^{-8}, and $10^{-9}\,\Omega\,\mathrm{cm}^2$. For the MIS contact, the effective metal workfunction of Ti was evaluated using the FLP attenuation module of Ref. 6. Whereas its ideal value is considered equal to 4.33 eV, the effective one was extracted at 4.35 eV in the case of the Al_2O_3 insertion.

One can see in Fig. 4(a), that the reverse current of the Al_2O_3-based MIS contact is found larger than the forward one. The degradation of the MIS contact forward current was attributed to the voltage drop occurring in the dielectric insertion when biasing the semiconductor in the accumulation regime [Fig. 4(b)]. This phenomenon has also been previously reported in experimental studies.[12]

From the previous observation, it follows that extracting the contact resistivity from a non-linear, non-symmetrical MIS junction can only be achieved by specifying the bias of extraction.

2.3 DC behavior

Yet, the effective operative contact bias to be considered arises from solving the voltage sharing between contacts and MOSFET when applying a supply voltage V_{dd}. *I–V* characteristics of 1D analytically-simulated MIS contacts were generated for several combinations of doping concentration, metallization, dielectric nature, and thickness. Elementary SPICE compact models were then fitted on these analytically simulated *I–V* characteristics and plugged on 10FDSOI p- and n-MOSFET blocks.

Including a built-in voltage-sharing, this protocol allows evaluating the MIS properties by directly looking at the performance of a MOSFET flanked by MIS contacts. Additionally, similar simulations can be performed for devices presenting the ideal ohmic references of 10^{-7}, 10^{-8}, and $10^{-9}\,\Omega\,\mathrm{cm}^2$ granting a straightforward benchmarking of the different configurations of MIS contact. The generated I_D–V_{DS} are presented in Fig. 5.

These results suggest that the effective contact resistivity value recommended by ITRS can be approached only on nFETs when using the insertion properties of Fig. 1. Indeed, the values reported in this figure indicate a lack of candidate with a low VBO.

Thanks to the simulations, it was also possible to extract the effective bias actually undergone by the contact when operating the MOSFETs under V_{dd}. This effective operative bias was extracted for Ti/Si, Ti/TiO_2/Si, and Zr/TiO_2/Si contacts and are shown in Fig. 6.

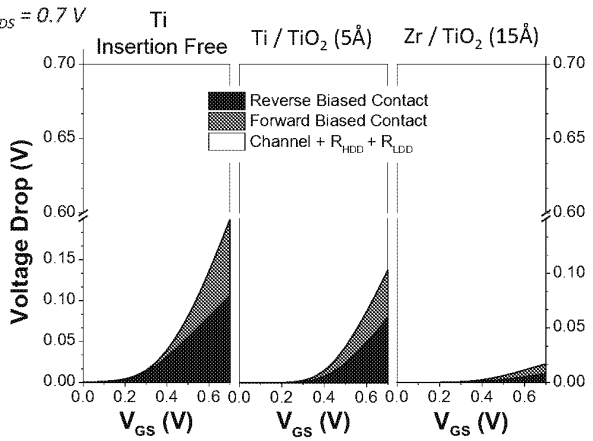

Fig. 6. (Color online) Sharing of V_{DS} voltage between the contacts and the transistor block for various contacts.[11]

The results highlight that the actual bias of the contact can vary in a wide range and thus cannot be automatically taken around zero.

2.4 AC behavior

DC characteristics improvement relying on equivalent contact resistivity reduction is a first figure of merit which can be used to evaluate the suitability of a MIS contact. Nevertheless, a dielectric insertion also results in what can be modeled by a capacitor in parallel with the contact diode (Fig. 7).

This capacitor may have a significant impact on the dynamic response of a transistor featuring MIS contacts. In order to probe the impact on the AC performance, seven-stage ring oscillators were implemented with different combinations of dielectric insertions. Their frequency of oscillation are plotted in Fig. 8.

It is interesting to note that while none of the diodes could perform as well as the $10^{-9}\,\Omega\,\mathrm{cm}^2$ limit in DC, the combination of Pt/p-Si and Zr/TiO_2 (15 Å)/n-Si outperforms it in the dynamic regime.

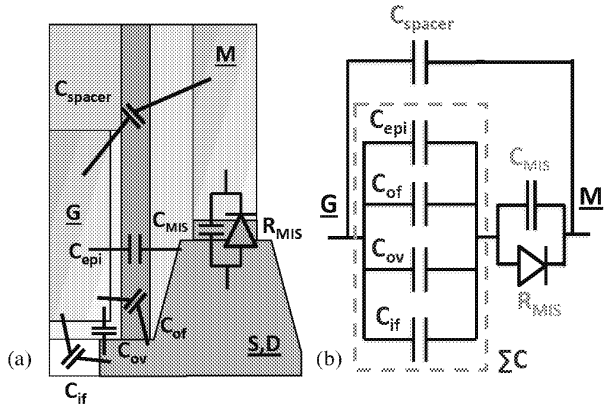

Fig. 7. (Color online) (a) Sketch of a transistor presenting the usual parasitic capacitances and the one induced by the dielectric insertion. (b) Equivalent electric block diagram.

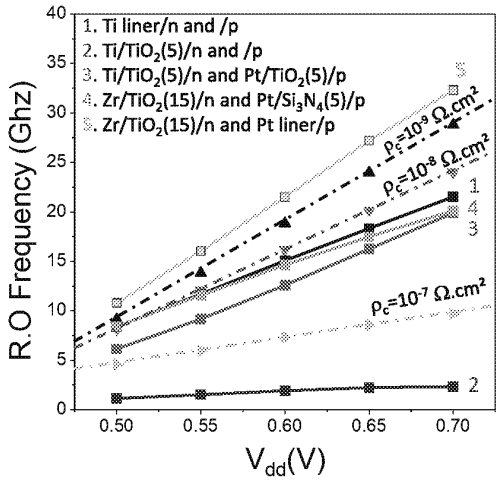

Fig. 8. (Color online) Seven-stage ring oscillator oscillation frequency as a function of the supply voltage with dielectric insertions.[13]

As explained in Ref. 13, the complex impedance modulus of a MIS contact is expressed by Eq. (2).

$$|Z_{eq}| = \frac{R^2}{1 + R^2 C^2 \omega^2} \tag{2}$$

At high frequency the capacitive nature of the dielectric insertion acts as a shunt to the resistor, hence reducing the conduction path impedance in the AC regime. Therefore, an additional gain may be obtained on the nFETs side thanks to their MIS contacts. Whereas these MIS contacts led to a performance just below the $10^{-9}\,\Omega\,cm^2$ mark in DC, this capacitive effect allows to surpass it in AC.

3. Electrical characterization concerns

As stated previously, extracting the contact resistivity from a non-linear and non-symmetrical MIS junction at an arbitrary bias without precising it can lead to a misrepresentation of this contact efficacy. Therefore extra caution is required in the choice of the electrical characterization test structure.

As presented in Fig. 9, three main structures can be retained: the back contact measurement, the transmission line method (TLM) and the cross bridge Kelvin resistor (CBKR);

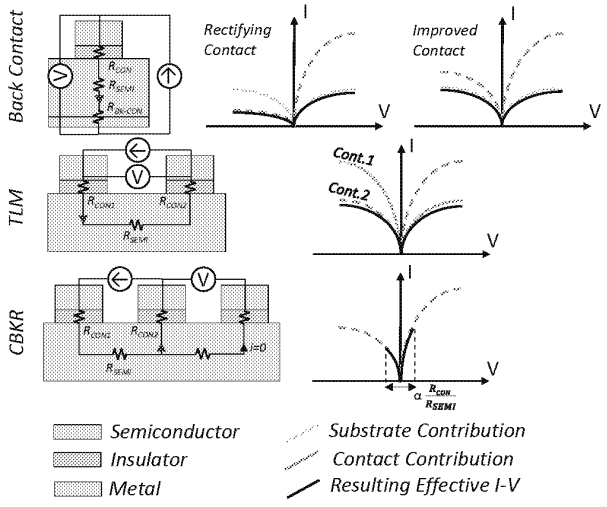

Fig. 9. (Color online) (Left) Main structures used to characterize the contact *I–V* and resistivity. (Right) Sketch of the associated *I–V* characteristics stressing the contributions of the different elements composing the test structure.[12]

each of them presenting its own advantages and drawbacks. For the sake of simplicity, only the equivalent 2D projection of the CBKR is plotted in this figure.

3.1 Back-contact structure

The back-contact measurement has been intensively used so far due to its simplicity of implementation and the straightforward *I–V* generation it offers. In order to show the transition from a Schottky behavior to an ohmic one, numerous studies have been focusing on the contacts *I–V* symmetry and linearity optimization using this technique as a measurement instrument of choice.

Nevertheless, as shown in Fig. 9, in this configuration the probed contact appears to be in series with the substrate. To some extent, and particularly when the target of the study is to reach an ultra-conductive contact, its resistivity can be negligible compared to that of the substrate.[14] Then the resulting current is limited by the latter and is no longer a signature of the former. An easy way to identify the discrepancy is that a TLM-extracted $10^{-8}\,\Omega\,cm^2$ value should normally translate into a current density of $10^8\,A/cm^2$ at 1 V. Yet, this value is never reached in back-contact measurements (typically saturating 6 orders of magnitude below), clearly showing that the actual contact behavior is screened by the measurement setup.

Simulations of this type of structure were performed in order to highlight the difference between the *I–V* of stand-alone Ti liner/n-Si and Ti/TiO_2/n-Si contacts compared with the measured *I–V* in a back contact test setup. The results are shown in Fig. 10. One can notice that the saturation due to the substrate prevents from evaluating properly the forward current of both contacts and leads to a contact asymmetry undervaluation. Therefore, even if introducing a dielectric layer truly improves the contact symmetry by increasing the reverse current, the figure could not be interpreted as an evidence of a transition from Schottky to ohmic behavior.

3.2 TLM or CBKR?

Widely used, the TLM can be utilized to easily extract the contact resistivity of a studied contact.[15] Nevertheless it

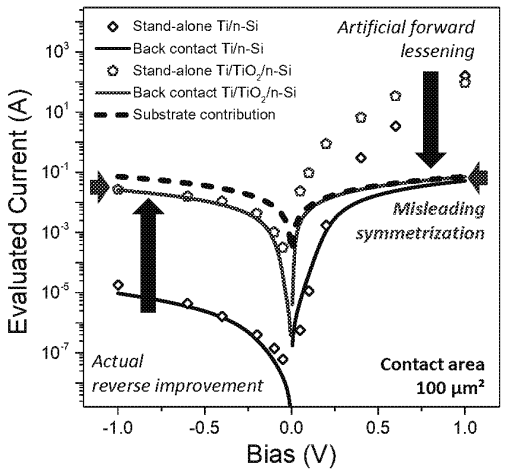

Fig. 10. (Color online) Comparison between *I–V* characteristics of a stand-alone contact based on a Ti liner and the corresponding curve measured in a back contact structure presenting a similar contact.

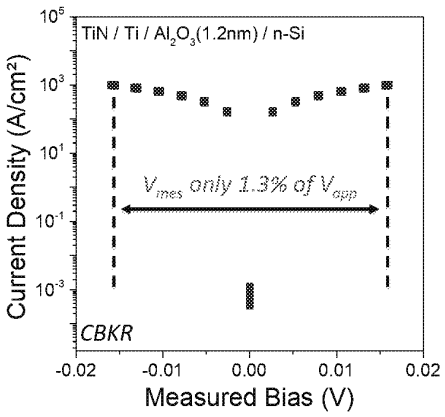

Fig. 11. (Color online) *I–V* characteristic of Al_2O_3-based MIS contacts. The contacts are only probed on a [−0.016; 0.016] range while the applied bias varied on [−1.2; 1.2].

regrettably loses this ability when the probed contact is not linear. Moreover, as shown in Fig. 9, its *I–V* characteristic is always dominated by the reverse of one of the two contacts required to implement the test structure. It thus artificially appears symmetric with no link on the contact symmetry. Therefore, it cannot be used to extract neither the contact resistivity nor the proper *I–V* characteristics from nonlinear contacts. Thus, this technique is arguably poorly adapted to characterize MIS contacts.

CBKR structures however allow in theory obtaining the whole *I–V* characteristics of the probed contact and thus is of prime interest to evaluate non-linear non-symmetrical contact like MIS contacts.[16] Nevertheless, for an ultra-low specific contact resistivity the real contribution of the contact begins to be negligible compared to that of the substrate. Two main effects arise in this configuration:

(i) The bias window in which the *I–V* of the contact can be plotted is reduced since a major part of the applied bias dropped in the substrate (Fig. 11). Indeed, if the contribution of substrate R_{sub} is high compared to that of the contact R_{co} then Eq. (3) becomes Eq. (4) and I_{app} is very low. Then the

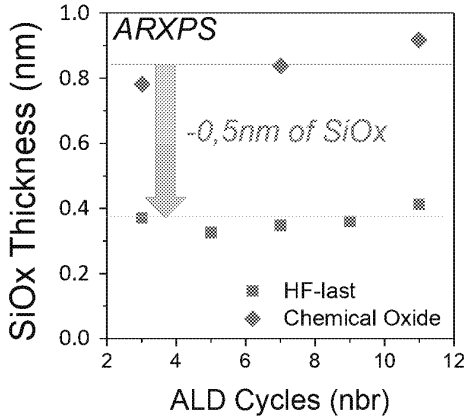

Fig. 12. (Color online) Native oxide regrowth occurring during Al_2O_3 ALD deposition evaluated using ARXPS.

probed bias V_{mes} remains a proper signature of the contact but is negligible itself.

$$V_{app} = R_{con} \times I_{app} + R_{sub} \times I_{app} \quad (3)$$

$$V_{app} \approx R_{sub} \times I_{app} \quad (4)$$

$$V_{mes} = R_{con} \times I_{app} \quad (5)$$

As an illustration, in Fig. 11 V_{mes} is only 1.3% of V_{app}. Therefore the main interest of the CBKR compare to the TLM that is obtaining a full *I–V* characteristics of the contact in order to evaluate its linearity is diminished.

(ii) Moreover, as the contribution of contact is lessened, Eq. (5) can no longer be applied in this form and becomes more complex. In order to account for the errors generated in the CBKR, two main models named 1D and 2D were developed to extract the specific resistivity. They can respectively be found in Refs. 17 and 18.

It appears that whereas back-contact measurement should not be used due to a likely screening of the contact characteristics by the substrate resistance, the TLM and CBKR techniques each present their own domain of validity.

4. Experimental results

After studying the fundamental aspects of the MIS contacts and evaluating the way to characterize them as accurately as possible, issues occurring during their practical implementation are presented. These concerns prevent from obtaining expected functioning ideal stack and add experimental constraints restricting the possible configurations. Several MIS contact configurations were implemented.

4.1 Substrate re-oxidation

SiO_2 presents both high conduction and valence band offsets (Fig. 1). Therefore, when treating MIS contacts, and particularly those on silicon, a proper passivation of the substrate has to be performed prior to the dielectric insertion since even a slight layer of native oxide could lead to a significant resistivity degradation.

Studies concerning the substrate re-oxidation during Al_2O_3 atomic layer deposition (ALD) were carried on using angle resolved X-ray photoelectron spectroscopy (ARXPS). The results are plotted in Fig. 12 and show that even though a HF-last cleaning process prior to the deposition leads to a 5 Å thinning of the SiO_2, a deposition induced light re-oxidation cannot be prevented.

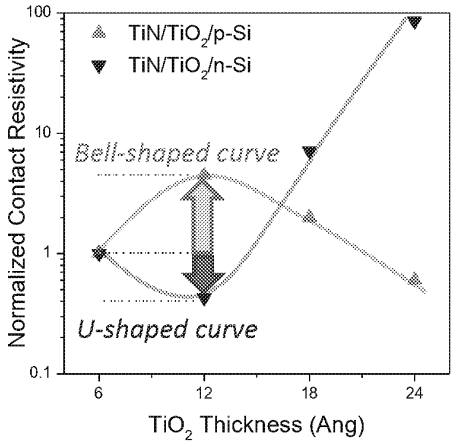

Fig. 13. (Color online) Contact resistivity of TiN/TiO_2/n- and p-Si as a function of the dielectric insertion. Contacts on p-Si feature a bell-shaped curve.

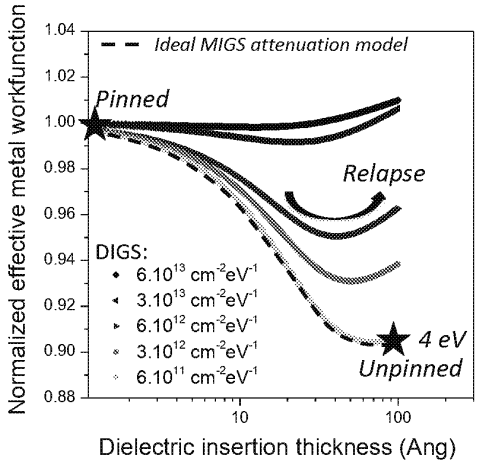

Fig. 14. (Color online) Effective metal workfunction as a function of the dielectric insertion considering various DIGS density at the semiconductor/dielectric interface.

Focusing on HfO_2 thin films,[19] it was shown that an additional innovative Cl_2 chlorine treatment should be added between the HF cleaning and the deposition in order to reduce the ALD induced re-oxidation. As stated in Ref. 19, whereas ALD deposition on top of an HF-passivated Si surface leads to 3D growth mode and induces interfacial oxide, ALD deposition on Cl_2-treated surface features only a 0.26 nm SiO_x regrowth that is corresponding to Si–O bonds at the HfO_2/Si interface. This type of surface treatment appears very promising for the optimization of MIS contacts.

4.2 Parasitic interface and bulk charges

Contacts based on TiO_2 insertion were fabricated on both n- and p-Si. Contact resistivity around 0 V were extracted using CBKR and are presented in Fig. 13. While the n-Si based contact resistivity features a classical U-shaped curve as predicted initially in Ref. 2, that of the p-type contacts follows a bell-shaped curve when increasing the dielectric insertion thickness.

Although such dependence has seldom been reported in the past, similar results can be found in Ref. 20. In this study, considering HfO_2 and TiO_2 based contacts, bell-shaped curves were obtained when introducing bulk charges in the dielectric inserted between a p-type metal and n-Ge.

In the simulation module used to evaluate the FLP, its intensity is calculated using interface charge model initially developed in Ref. 21. The link between the slope parameter S and the charge density is described by Eq. (6). The slope parameter can be understood in terms of how efficiently a variation of ideal workfunction (i.e., change of material) affects the effective workfunction.

$$S = \frac{d\Phi_m^{eff}}{d\Phi_m} = \frac{\varepsilon_{sc}}{\varepsilon_{sc} + q^2\delta D_{it}} \tag{6}$$

where Φ_m^{eff} is the effective metal workfunction, Φ_m is the ideal one, ε_{sc} is the permittivity of the considered semiconductor (here Si), and D_{it} is the density of the interface charge.

So far the interface charges were attributed solely to MIGS without considering any fixed charge induced by defects, also called defects induced gap states (DIGS). Nevertheless this type of model could not predict the results obtained in Fig. 13, in particular the bell-shaped curve.

As presented in Eq. (7), using analytical simulation, charges were introduced at the interface between the dielectric and the substrate in order to account for the DIGS contribution.

$$S = \frac{\varepsilon_{sc}}{\varepsilon_{sc} + q^2\delta(D_{MIGS} + D_{DIGS})} \tag{7}$$

A notional case was studied considering a metallization with an ideal workfunction of 4 eV. The variation of the effective workfunction as function of the dielectric thickness was generated for different interface charge densities. In Fig. 14, the effective metal workfunction normalized by its value without dielectric insertion, and thus complete FLP, is plotted as a function of the dielectric thickness for the different DIGS density.

Regardless of the DIGS density, the metal workfunction always starts at a complete FLP for ultra-low dielectric thickness. At low DIGS densities, the variation of the effective metal workfunction is close to the trend predicted by an ideal MIGS attenuation model (dashed line). Then for a thick enough dielectric, the FLP is totally mitigated, the effective workfunction tends towards the ideal one (4 eV), making such a contact suitable for n-type Si.

However, when the parasitic gap states are dominated by the DIGS rather than the MIGS, a relapse is observed after a first decrease of the effective metal workfunction. When considering a negligible tunneling resistance in the TiO_2 layer, such a variation would lead to a bell-shaped curve on p-type substrates and thus could explain the experimental results of Fig. 13.

This is an indication that the respective contributions of DIGS and MIGS to the Fermi level pinning phenomenon still have to be investigated, since a pure MIGS-based model fails to explain particular trends like the bell-shaped curve.

4.3 Metallization and insertion stability

Once the dielectric insertion is performed, the junction needs to be completed by the deposition of the metallic top electrode. Contacts based on n-Si should be connected to a low work function metal in order to fully benefit from the FLP mitigation. However, most "n-type" metals are well known to be oxygen getters. Therefore, fabricating a MIS

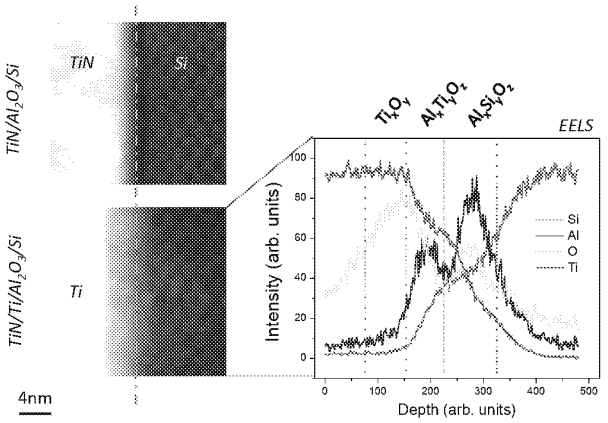

Fig. 15. (Color online) (Left) Transmission electron microscopy observations of Al_2O_3-based MIS contact stacks, using either TiN or Ti as a capping metal, showing in the latter case Ti diffusion through the insertion. (Right) Electron energy loss spectroscopy corresponding to the $Ti/Al_2O_3/Si$ contact annealed at 440 °C.

contact composed by n-metal/insulator/n-semiconductor without degrading the dielectric insertion after undergoing BEOL thermal budget is an additional challenge.[22] Capping metals with high diffusivity may also jeopardize the integrity of the contact stack. In Ref. 22, the destruction of a TiO_2 insertion was observed when using Ti metallization to complete the MIS contact. Although being one of the first studies to present such phenomenon, the studied contact presents a binary system composed of Ti and O. Similar experiments should be extended to more complex configurations such as ternary or quaternary systems.

In order to investigate such phenomenon, the classical TiN/Ti metallization[23] was implemented on top of an Al_2O_3 insertion as long as solely TiN capping metal. The metallic electrode was completed by a CVD W deposition at 440 °C. Results of Fig. 15 show that while the TiN metallization seems to ensure the MIS contact stability, the CVD thermal budget is enough to trigger a reaction between Ti and Al_2O_3. Interestingly the signal of Al features two separate peaks indicating the splitting of the Al_2O_3 layer into an $Al_xTi_yO_z$ and an $Al_xSi_yO_z$ layers. One can also notice that the O diffuses further in the Ti than the boundary of the $Al_xTi_yO_z$ layer.

5. Conclusions

MIS contacts present the counter-intuitive potential for decreasing the contact resistivity by an insulator insertion.

Their efficiency, relying on SBH modulation, is however toned down in a field-emission-dominated regime and then is diminished at high doping concentration. Gauging this efficiency is moreover not straightforward since such contacts are non-linear and dissymmetric, so that evaluating their equivalent resistivity requires knowing their full *I–V* behavior and self-consistently solve their operative bias. This output characteristic cannot be obtained using back contact structure or TLM. Thus, even presenting a reduced probing range, CBKR should be privileged.

According to modeling and simulations in the DC regime, it seems that commonly used dielectrics are not adapted for p-type contacts due to large Band Offsets and that optimal cases on n-type Si only lead to performance below the ITRS target of $10^{-9}\,\Omega\,cm^2$. Interestingly, AC behavior of MOSFETs seems to come with an additional boost due to a shunt capacitor effect of the MIS contact and to feature performance above this limit value.

Concerning the n-type contact, two challenges remain for practical implementation: avoiding SiO_2 regrowth during the dielectric deposition, and limiting the interactions (scavenging, diffusion) with the low work function capping metal.

Finally, experimental results on TiO_2 insertions display an inverse bell-shaped curve which cannot be explained by the traditional MIGS attenuation model. Considering DIGS, it seems possible to reproduce this behavior by simulation.

Acknowledgements

This work was partially carried out in the frame of the ST-Leti joint program. It was also partly funded by the French Public Authorities through NANO 2017 program and through Equipex FDSOI11.

1) T. Nishimura, K. Kita, and A. Toriumi, Appl. Phys. Lett. **91**, 123123 (2007).
2) D. Connelly, C. Faulkner, D. E. Grupp, and J. S. Harris, IEEE Trans. Nanotechnol. **3**, 98 (2004).
3) P. P. Manik, R. K. Mishra, V. P. Kishore, P. Ray, A. Nainani, Y.-C. Huang, M. C. Abraham, U. Ganguly, and S. Lodha, Appl. Phys. Lett. **101**, 182105 (2012).
4) S. Gupta, P. P. Manik, R. K. Mishra, A. Nainani, M. C. Abraham, and S. Lodha, J. Appl. Phys. **113**, 234505 (2013).
5) J. Robertson, Appl. Surf. Sci. **190**, 2 (2002).
6) J. Borrel, L. Hutin, O. Rozeau, M.-A. Jaud, S. Martinie, M. Gregoire, E. Dubois, and M. Vinet, IEEE Trans. Electron Devices **63**, 3413 (2016).
7) J. Borrel, L. Hutin, O. Rozeau, M.-A. Jaud, S. Martinie, M. Gregoire, E. Dubois, and M. Vinet, IEEE Trans. Electron Devices **63**, 3419 (2016).
8) H. B. Michaelson, J. Appl. Phys. **48**, 4729 (1977).
9) J. Wright, R. Khanna, L. F. Voss, L. Stafford, B. Gila, D. Norton, S. Pearton, F. Ren, and I. I. Kravchenko, ECS Trans. **6** [2], 279 (2007).
10) M. K. Niranjan, S. Zollner, L. Kleinman, and A. A. Demkov, Phys. Rev. B **73**, 195332 (2006).
11) J. Borrel, L. Hutin, O. Rozeau, P. Batude, T. Poiroux, F. Nemouchi, and M. Vinet, Symp. VLSI Technology, 2015, T116.
12) J. Borrel, L. Hutin, H. Grampeix, E. Nolot, M. Tessaire, G. Rodriguez, Y. Morand, F. Nemouchi, M. Grégoire, E. Dubois, and M. Vinet, Int. Workshop Junction Technology, 2016, p. 14.
13) J. Borrel, L. Hutin, O. Rozeau, M.-A. Jaud, S. Martinie, E. Dubois, and M. Vinet, IEEE Semiconductor Interface Specialists Conf., 2015.
14) J. H. Werner, Appl. Phys. A **47**, 291 (1988).
15) H. H. Berger, Solid-State Electron. **15**, 145 (1972).
16) S. J. Proctor, L. W. Linholm, and J. A. Mazer, Trans. Electron Devices **30**, 1535 (1983).
17) M. Ono, A. Nishiyama, and A. Toriumi, Solid-State Electron. **46**, 1325 (2002).
18) N. Stavitski, J. H. Klootwijk, H. W. van Zeijl, B. K. Boksteen, A. Y. Kovalgin, and R. A. M. Wolters, Technology Foundation STW, 2007, p. 551.
19) J.-F. Damlencourt, O. Renault, A. Chabli, F. Martin, M.-N. Séméria, and F. Bedu, J. Mater. Sci.: Mater. Electron. **14**, 379 (2003).
20) A. M. Roy, Dr. Thesis, Stanford University, Stanford, CA (2012).
21) W. Monch, Rep. Prog. Phys. **53**, 221 (1990).
22) H. Yu, M. Schaekers, E. Rosseel, A. Peter, J.-G. Lee, W.-B. Song, S. Demuynck, T. Chiarella, J.-Å. Ragnarsson, S. Kubicek, J. Everaert, N. Horiguchi, K. Barla, D. Kim, N. Collaert, A. V.-Y. Thean, and K. De Meyer, IEDM Tech. Dig., 2015, 21.7.1.
23) T. Maeda, T. Nakayama, S. Shima, and J. Matsunaga, IEEE Trans. Electron Devices **34**, 599 (1987).